Magnetic reconnection and plasma dynamics in two beam laser-solid interactions

†P. M. Nilson, L. Willingale, *M. C. Kaluza, C. Kamberidis, #M. S. Wei, P. Fernandes, R. J. Kingham, Z. Najmudin, M. G. Haines, A. E. Dangor and ‡K. Krushelnick

Department of Physics, The Blackett Laboratory, Imperial College London, London, SW7 2AZ, UK

M. Notley, S. Bandyopadhyay, M. Sherlock and R. G. Evans

Central Laser Facility, CCLRC Rutherford Appleton Laboratory, Chilton, Didcot, Oxon., OX11 0QX, UK

S. Minardi and M. Tatarakis

Technological Educational Institute of Crete, Chania, Crete, Greece

W. Rozmus

Department of Physics, University of Alberta, Edmonton, Alberta, Canada

†Present address: Laboratory for Laser Energetics, University of Rochester, 250 East River Road, Rochester, NY, USA.
*Present address: Institute for Optics and Quantum Electronics, Max-Wien-Platz 1, D-07743 Jena, Germany.
#Present address: Center for Energy Research, University of California, San Diego, CA 92093-0417, USA.
‡Present address: Center for Ultrafast Optical Science, University of Michigan, Ann Arbor MI, USA.

Main contact email address: philip.nilson@imperial.ac.uk

Introduction

Magnetic reconnection describes the breaking and reconnecting of magnetic field lines in a plasma that allows previously isolated magnetic field distributions to become connected[1]. In a magnetized plasma the process of reconnection converts magnetic energy into bulk plasma heating and fast particle production and can have a significant impact on the plasma dynamics.

Reconnection processes occur on short timescales. Much effort has been given to explaining the cause of rapid energy release, which has been attributed to reconnection, its triggering mechanisms, and the resulting bulk plasma heating and high energy particle production[2]. There are two main approaches to this problem. The Sweet-Parker model[3] requires the formation of a current sheet, while the Petschek model[4] uses a pair of slow-mode magnetohydrodynamic (MHD) shocks. Each approach is based on two dimensional incompressible MHD theory.

Central to magnetic reconnection is the formation of a neutral current sheet due to hydromagnetic flows. At neutral current sheets the plasma flow velocity $\mathbf{u} = 0$ and the electric field $\mathbf{E}$ is balanced by $\eta\mathbf{J}$, where η is the resistivity and $\mathbf{J}$ is the current density. In this region diffusion can become very large and the magnetic field can reconnect and give rise to large $\mathbf{J} \times \mathbf{B}$ forces. The introduction of a small but finite resistivity allows the magnetic field to be decoupled from the bulk plasma motion and the plasma to move across lines of magnetic flux. In consequence, the magnetic field lines in a plasma are able to reorganise themselves and release energy, which can then be converted into other forms.

Magnetic reconnection has been studied in the Earth's magnetosphere, at the solar surface, and during major and minor disruptions in magnetic confinement fusion devices[5,6]. Its role in multiple laser beam geometry experiments has not previously been considered. A clear motivation and environment in which this may occur and be dynamically important upon electron transport is the inner hohlraum wall surface[7,8].

The experimental rationale for the work presented here was to investigate whether or not a magnetic reconnection geometry could be created in the laboratory using two moderate intensity heater beams that are focused in close proximity to each other on a solid target. Our idea is presented in figure 1, where the self-generated magnetic fields around each heater beam focal spot interact and form a reconnection layer.
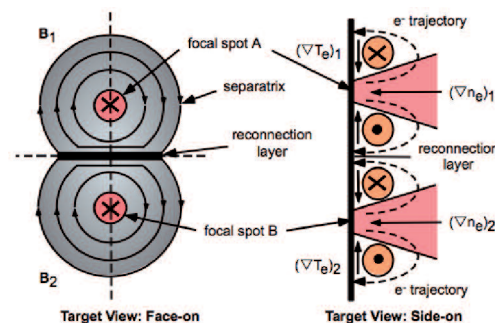

Figure 1. The target and field configuration of a self-generated magnetic reconnection geometry in a laser-produced plasma using two heater beams.

Many open questions remain in the field of magnetic reconnection, including the rate at which reconnection proceeds, field-aligned jet formation, the microphysics of the heating mechanisms present, the role of shock waves, and the resistive mechanisms that facilitate the conversion of magnetic energy into bulk plasma motion and particle acceleration[1]. The open geometry available in a laser-produced magnetic reconnection geometry may help elucidate some of these fundamental issues.

Experimental Method

Two heater beams, with wavelength $\lambda = 1.054$ μm, were used to irradiate either an aluminium or gold target foil that was 3 mm × 5 mm and 20 – 100 μm thick. A 1 ns duration square pulse was used with an average energy of 200 J per beam. The energy in each beam was verified using a full beam diameter calorimeter prior to the beam

entering the target chamber to account for any losses due to poor mirror quality. Each beam was focused using f/10 optics to a focal spot diameter of 30 – 50 µm FWHM, giving an incident laser intensity of 1×10^{15} Wcm^{-2}. The focal spot quality was verified using time-integrated x-ray pinhole imaging.

The two heater beams were aligned with varying on-target separations of up to ten times the focal spot diameter. Figure 2 shows the interaction chamber. This diagram shows the orientation of the two heater beams and their focusing geometry with respect to the other diagnostic beams.
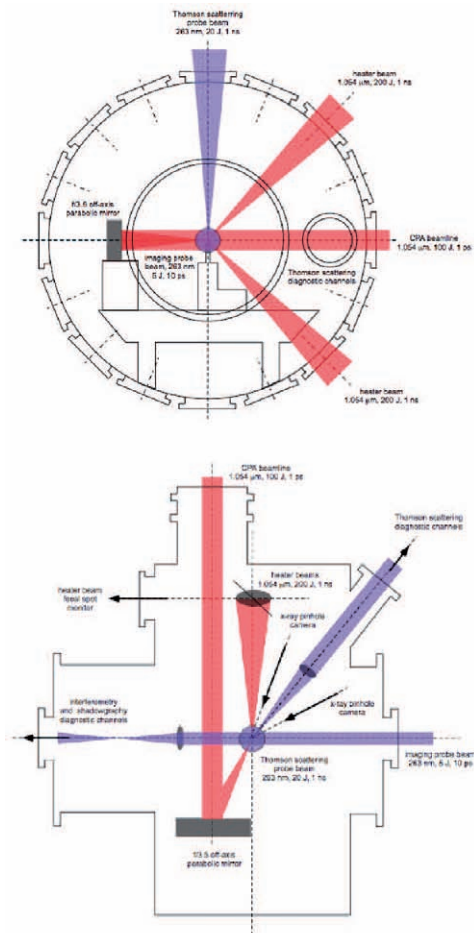

Figure 2. The TAW interaction chamber. The heater beam, the 263 nm probe beam, the CPA beam, and the 263 nm Thomson scattering probe beam alignment are shown. The diagnostic channels and the two x-ray pinhole cameras are indicated.

The probe beam was frequency converted to 263 nm and aligned transverse to the target foil. The final compression gratings were located in air and resulted in the probe pulse having a 10 ps pulse duration. The beam was also aperture limited to a diameter of 10 mm.

The probe beam light refracted by the target plasma was re-imaged outside the interaction chamber. Two and three lens imaging systems were used throughout this work that provided various image magnifications of around 13×. An external, 10 Hz frequency quadrupled Nd:YAG laser operating in the UV was incorporated into the system and aligned co-linear to the main Vulcan probe beam to allow off-line adjustments.

The probe beam diagnostic channels included a modified Nomarski interferometer and a shadowgraphy channel. High dynamic range, 16 bit Andor cameras were used as detectors on each channel and incorporated a combination of reflective and bandpass ($\Delta\lambda = 10$ nm) interference filters to reduce the detectable self-emission from the target.

Two x-ray pinhole cameras were used to monitor the time-integrated x-ray emission from the laser focal spots and the interaction region. One camera viewed the target approximately face-on and the other viewed the interaction approximately side-on. Their oblique viewing angles were dictated by the location of the heater and probe beams. Each camera incorporated 20 – 50 µm diameter pinholes and were filtered with 20 µm of Mg that gave a sensitivity to around 1 keV x-ray emission with a magnification of approximately 15×. The cameras used Kodak DEF film.

Magnetostatic and electrostatic field effects were studied using proton grid deflectometry. The protons were derived from a 20 µm thick gold foil located 2 mm behind the main target. The high intensity, 1 ps pulse duration CPA beam, with an energy of 100 J, was focused onto the gold foil using an f/3.5 off-axis parabolic mirror. A peak intensity of 5×10^{19} Wcm^{-2} was achieved with a focal spot of 8 – 10 µm FWHM, containing 30-40% of the energy. The proton source foil was fixed to a washer, as shown in figure 3 behind the main target. The proton flux was projected through the rear of the main target and detected using a stack of filtered radiochromic film (RCF). Prior to reaching the main target, the proton flux passed through a 25 µm × 25 µm mesh located on the other side of the washer. Magnetostatic and electrostatic fields distort the image of the mesh as it passes through the target plasma prior to being detected. The distance between the proton source and the mesh was 1 mm. The main target was a further 1 mm away, while the distance between the main target and the RCF detector was 20 mm. The final image magnification was 10×.
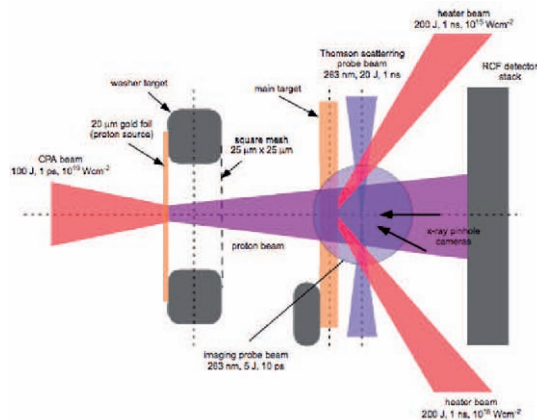

Figure 3. The target configuration, heater beam alignment, diagnostic beams and diagnostic viewing angles.

Thomson scattering (TS) was used to measure the electron temperature at various locations in the target plasma. The system used a 10 J, 263 nm probe beam of 1 ns (square) pulse duration. The probe beam was aligned parallel to the target surface and focused to 50 µm using f/10 optics. Scattered light was collected at $\theta = 90°$ and re-imaged with a magnification of 1.5× upon a 100 µm spectrometer slit. The Thomson scattered light was spectrally dispersed

using a 3600 lines/mm grating and a 1 m spectrometer coupled to a streak camera. The time-resolved TS spectra were measured with a temporal resolution of 100 ps and a wavelength resolution of 0.05 nm. For typical electron densities and temperatures in open foil geometries, collective TS spectra are expected; the scattering parameters are $\alpha = 1/k\lambda_D \approx 2$, where α is the scattering vector and λ_D is the Debye length.

Results

263 nm probing

Figure 4 shows a shadowgram of an aluminium target interaction taken at $t = t_0 + 1.5$ ns (left) and a shadowgram of a gold target interaction taken at $t = t_0 + 2.0$ ns (right). The time at which the heater beams first reach the target surface is defined as t_0. These interactions were created using two heater beams with a laser spot separation on the target surface of around 150 µm. Each of these interactions show similar plasma evolution. The plasma generated at each of the laser spots has expanded both transversely and perpendicularly to the target surface and met the plasma generated by the other laser spot at the midplane between the two. In figure 4 the plasmas have collided in each case and formed a quasi-homogeneous blow-off plasma plume. Figure 5 shows two dimensional electron density maps of these interactions. Cylindrical symmetry has been assumed around the centre of the interactions and an Abel transformation has been used to recover the electron density values. For each material, the plasma expansion occurs in a region of approximately
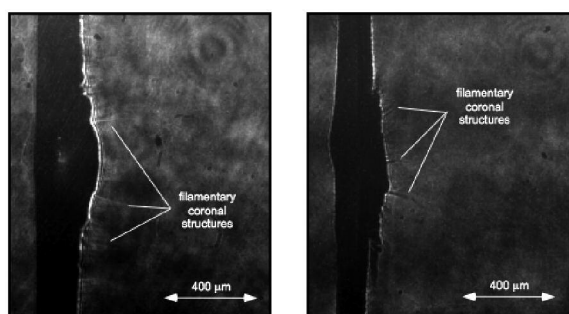

Figure 4. Shadowgrams of an aluminium (left) and gold (right) target interaction taken at $t = t_0 + 1.5$ ns (left) and a shadowgram of a gold target interaction taken at $t = t_0 + 2.0$ ns (right).
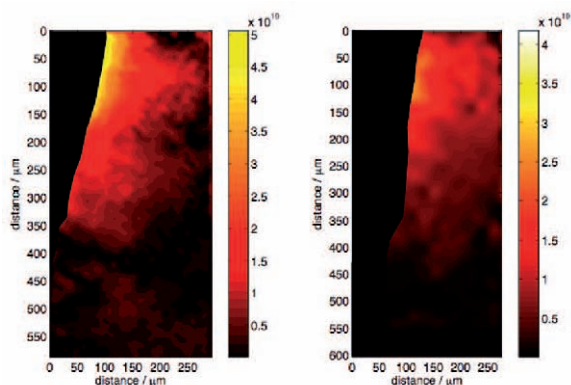

Figure 5. Two dimensional electron density maps of the aluminium target interaction shown in figure 4 (left) taken at $t = t_0 + 1.5$ ns (left) and the gold target interaction shown in figure 4 (right) taken at $t = t_0 + 2.0$ ns (right).

600 µm in extent that is centred around the midplane and has created a coronal region of typical electron densities of around $n_e = (1\text{-}3) \times 10^{19}$ cm^{-3} that extends many hundreds of microns perpendicular to the target surface. The expansion velocities that are achieved perpendicular to the target for each material are of the order of 10^7 cms^{-1}.

A shadowgram from an aluminium interaction, taken at $t = t_0 + 1.5$ ns, is shown in figure 6 (left). The focal spot separation is around 400 µm. The darker areas correspond to regions, which are opaque to the probe light, and also regions where there are large density gradients. The two laser ablated plumes are clearly identifiable with a very prominent flow of plasma in between, propagating at $v_\perp \approx 5 \times 10^7$ cms^{-1} away from the target surface.

Similar dynamics are found for gold targets. Figure 6 (right) shows plasma outflows at $t_0 + 2.5$ ns. The central plasma feature is not a stagnation column, but the transverse projection of two high velocity jets, as shown in figure 7.
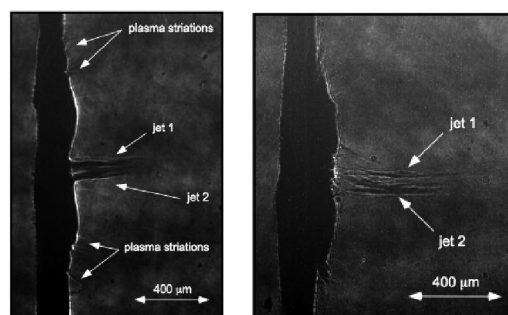

Figure 6. Shadowgrams of an aluminium target interaction taken at $t = t_0 + 1.5$ ns (left) and a gold target interaction taken at $t = t_0 + 2.5$ ns (right).
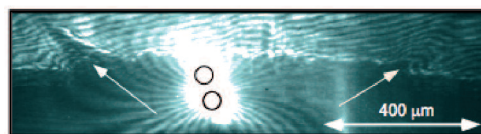

Figure 7. An interferogram of a gold target interaction taken at $t = t_0 + 0.7$ ns. The image shows an oblique viewing angle of the target surface. The focal spots are marked with black circles (not to scale).

Figure 8 (top) shows a simultaneous interferogram of the interaction shown in figure 6 (right). This image shows the highly collimated nature of the jets and a distinct oscillation as they propagate. Localised fringe shifts along the length of jet 2 appear to show jet collimation as it propagates and may be a contributing factor to the apparent oscillation. Figure 8 (bottom) shows a two dimensional electron density phase map of jet 1. Only the outer 250 – 300 µm of the jet has been considered. Cylindrical symmetry has been assumed and an Abel transformation has been performed to recover the electron densities. Indeed such approximations are not completely valid in this case. An overestimate of the electron density will be produced and consideration of non-cylindrically symmetric flows is not accounted for. Nonetheless such an analysis demonstrates a higher density central region to the jet that remains relatively well collimated for hundreds of microns.

Figure 9 shows an interferogram of another gold interaction using laser spots separated at the target surface by 400 µm.
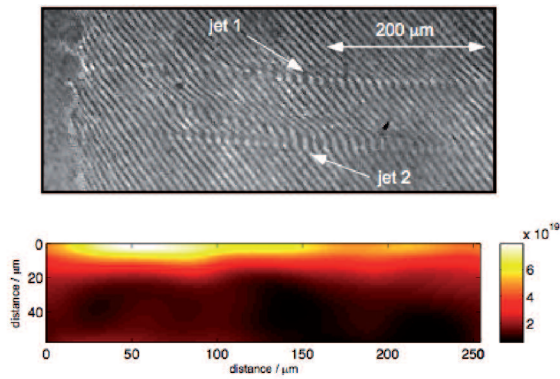
Figure 8. An interferogram (top) of the two outflowing jets shown in figure 6 (right) taken at t = t$_0$ + 2.5 ns. A two dimensional electron density map of jet 1 (bottom). Only the outer 250 μm of the jet is considered.
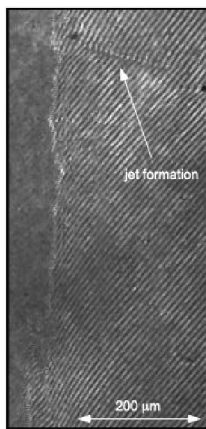

Figure 9. An interferogram of a gold target interaction taken at t = t$_0$ + 2.0 ns. A single highly collimated jet is observed to extend away from the target surface (the second jet expected to appear on the opposing side of the target is beyond the viewing angle of the detector on this shot).
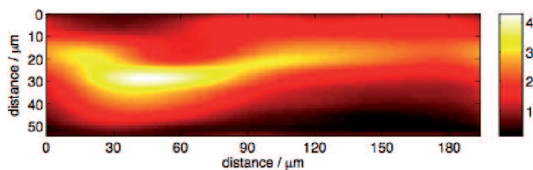

Figure 10. A phase map of the outflowing jet that is created during the gold target interaction shown in figure 9 taken at t = t$_0$ + 2.0 ns. The phase map scale is in radians.

The image is taken at t = t$_0$ + 2.0 ns. Here an outflowing jet has formed at a relatively large angle with respect to the probe beam. The second jet that is expected to form on the opposite side of the target is not in the viewing angle of the camera on this shot. This means that a clear image of a single jet has been produced. The jet is around 150 μm in extent and highly collimated. A phase map of the outflowing jet is shown in figure 10 and demonstrates the presence of jet narrowing and non-symmetric flows.

Proton deflectometry

Typical proton imaging data are shown in figure 11 and figure 12 for aluminium target interactions. Figure 11 shows an image sensitive to 13.5 MeV protons taken at
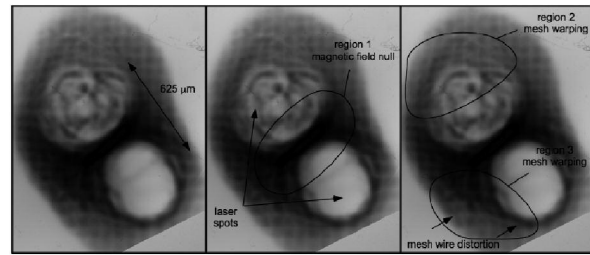

Figure 11. A proton deflectometry image sensitive to 13.5 MeV protons of an aluminium target interaction using two heater beams. The image is taken at t = t$_0$ + 0.1 ns and has been annotated on three replica images for clarity.
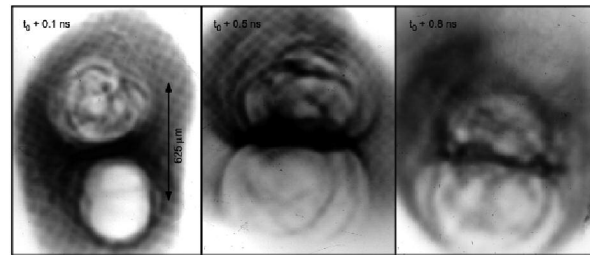

Figure 12. Proton deflectometry images of an aluminium target interaction using two heater beams. The images are taken at t = t$_0$ + 0.1 ns (13.5 MeV protons), t = t$_0$ + 0.5 ns (11.0 MeV protons), and t = t$_0$ + 0.8 ns (7.0 MeV protons).

t = t$_0$ + 0.1 ns. The image has been annotated on three duplicate images for clarity. By t = t$_0$ + 0.1 ns, protons have been radially deflected away from each of the laser spots by the self-generated $\nabla T_e \times \nabla n_e$ azimuthal magnetic fields. Proton density perturbations in the blow-off plasma regions are caused by the localised electric and magnetic fields associated with fine-scale filamentary structures at the target surface and in the coronal plasma. A region of proton accumulation is observed in region 1 at the midplane between the two laser spots. This is consistent with the azimuthal magnetic fields deflecting protons into the region of magnetic field null. Region 2 and region 3 shows distortion of the mesh image due to magnetic field effects.

In this face-on configuration, the dominant electric field is in the target normal direction $\mathbf{E} = E\mathbf{z}$ and the protons are deflected by the $\mathbf{v} \times \mathbf{B}$ force. This assumption is shown to be valid by considering the magnitude of the radial electric field. In the vicinity of the laser spot the electron temperature $T_e \approx 1$ keV reduces over a characteristic lengthscale $L_T \approx 100$ μm. The electric field is therefore estimated to be $E \approx 10^7$ Vm^{-1}. In comparison to the magnetic force term in the Lorentz equation, $vB = 3 \times 10^9$ Vm^{-1} for a 100T magnetic field and a 10 MeV proton with a velocity $v_p = 4.5 \times 10^7$ ms^{-1}.

Figure 11 shows grid deflections of around 25 μm. This corresponds to an apparent deflection in the detector plane of around 500 μm. An apparent grid deflection of 500 μm in the detector plane for protons of around 13.5 MeV indicates a magnetic field of around 1.3 MG assuming the self-generated magnetic field has expanded 100 μm perpendicular to the target surface. Such conditions and the range of imaged grid deflections around the laser focal spot edges indicate magnetic fields in the range 0.7 - 1.3 MG at t = t$_0$ + 0.1 ns.

Figure 12 shows proton deflectometry images taken at $t = t_0 + 0.1$ ns (13.5 MeV protons), $t = t_0 + 0.5$ ns (11.0 MeV protons), and $t = t_0 + 0.8$ ns (7.0 MeV protons). By $t_0 + 500$ ps, the magnetic fields generated in the plasma have expanded across the target surface at around 10^7 cms^{-1} and have started to interact with each other. At later times, the thin interaction region of around 100 μm thickness develops instabilities, characteristic of the azimuthal magnetic fields, counterstreaming flows and velocity shear present. It is clear that the plasma is magnetized and the presence of the magnetic fields are greatly affecting the plasma dynamics in this region.
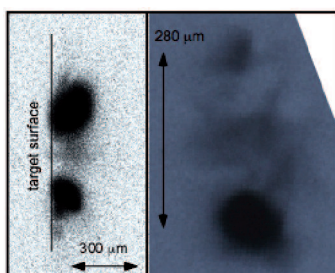
X-ray pinhole imaging

Figure 13. Time-integrated x-ray pinhole imaging of gold target interactions transverse (left) and face-on (right) to the main target surface.

Figure 13 shows two pinhole camera images of gold target interactions. The transverse image (left) shows significant emission from each of the ablated plasmas created by the laser spots. A central region of emission is observable in the midplane. Localised emission is also observable at the extremeties of the target. This emission is likely due to electrons returning to the target surface and causing localised heating. The face-on view (right) also shows emission from each of the laser spots and the midplane. Emission from the midplane is not purely planar in extent but also exhibits striations of hot plasma at the boundaries.
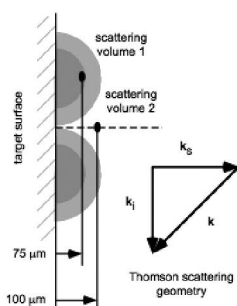
Thomson scattering

Figure 14. A diagram of the Thomson scattering geometry.

Figure 14 shows the two locations where TS light was collected from. Each region was scattered from on different shots. Scattering volume 1 was located 75 μm from the target surface in the centre of a single laser ablated blow-off plasma plume. Scattering volume 2 was located 100 mm from the target surface equidistant from each of the two heater beam laser spots. This is where the two laser ablated plasmas interact with each other.
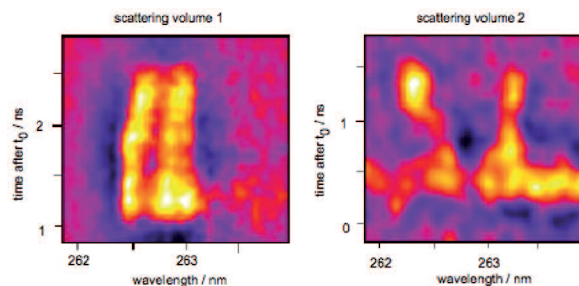

Figure 15. Time resolved Thomson scattering spectra from scattering volume 1 (left) and scattering volume 2 (right).
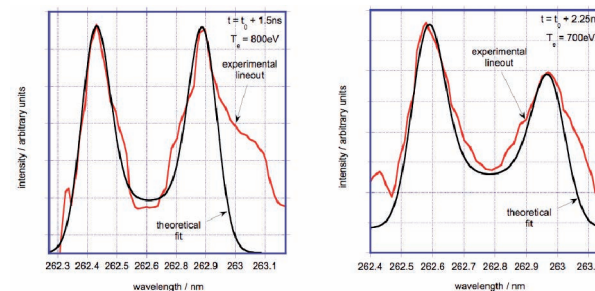

Figure 16. Lineouts of the experimental Thomson scattering spectrum (red) from scattering volume 1 at $t = t_0 + 1.5$ ns (left) and $t = t_0 + 2.25$ ns (right). The spectrum is fitted with the standard collisionless theory of the dynamic form factor given (black). Such theoretical fits give estimates of the electron temperature $T_e = 800$ eV at $t = t_0 + 1.5$ ns and $T_e = 700$ eV at $t = t_0 + 2.25$ ns.

Figure 15 (left) shows a temporally resolved TS spectrum from scattering volume 1. For $t_0 + 1.0$ ns $< t < t_0 + 2.0$ ns, two ion acoustic features are observed from light scattering from the aluminium plasma. The separation between the two features reduces in time indicating a decreasing electron temperature from hydrodynamic expansion.

Figures 16 shows experimental lineouts (red) of the spectrum at $t = t_0 + 1.5$ ns (left) and $t = t_0 + 2.25$ ns (right) with theoretical fits (black) that have been obtained from the standard collisionless theory of the dynamic form factor [9].

The electron and ion velocity distribution functions are Maxwellians, the electron density $n_e = 5 \times 10^{19}$ cm^{-3} and the fits include experimental broadening related to the wavelength resolution of the spectrometer $\Delta\lambda = 0.05$ nm. The separation between the two ion acoustic resonances in figure 16 is consistent with electron temperatures $T_e = 800$ eV (left) and $T_e = 700$ eV (right), respectively. The slight asymmetry in the ion acoustic peaks in figure 16 (right) is modelled by an electron drift velocity of $u_d = 3.0 \times 10^7$ cms^{-1}. Such a drift of the bulk electrons may occur in response to the heat flux carried by fast particles. Typical estimates of the error that is introduced in TS analysis is 10-20 %.

Figure 15 (right) shows a temporally resolved TS spectrum from scattering volume 2. This is the region of the plasma expansion where electrons are not directly heated by the laser beams. A large increase in the ion acoustic peak separation for $t > t_0 + 1.0$ ns is observed. For an equilibrium plasma (Maxwellian electron and ion velocity distribution functions), a straightforward fit of the

experimental scattering spectrum (red) in figure 17 (left) at $t = t_0 + 1.2$ ns to the scattering form factor results in the electron temperature $T_e = 5.4$ keV. An electron density $n_e = 2.5 \times 10^{20}$ cm^{-3} was required to obtain a good theoretical fit. Setting the electron temperature equal to the ion temperature was also assumed. The fit includes experimental broadening related to the wavelength resolution of the spectrometer $\Delta\lambda = 0.05$ nm.
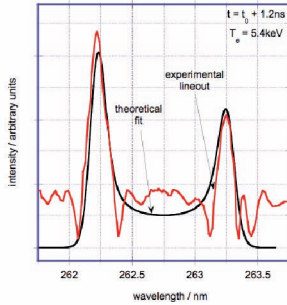

Figure 17. A lineout of the Thomson scattering spectrum (red) from scattering volume 2 at $t = t_0 + 1.2$ ns. The spectrum is fitted with the standard collisionless theory of the dynamic form (black) resulting in an estimate of the electron temperature $T_e = 5.4$ keV.

While investigating the parameter space that provided good experimental fits an electron temperature as high as $T_e = 9$ keV was predicted using an electron density $n_e = 1.0 \times 10^{20}$ cm^{-3} and setting the electron temperature a factor two above the ion temperature. In addition, the above theoretical fits require electron drift velocities of a few 10^8 cms^{-1} to reconcile the asymmetry in the peaks of the experimental scattering spectrum.

Discussion

In the previous section a number of observations were presented of a target plasma created at the surface of a solid target using two heater beams. It has been shown that the target plasma evolution is particularly sensitive to the laser spot separation. When the laser spots are around 150 μm apart the plasmas collide and form a quasi-homogeneous blow-off plasma. When the laser spot separation is increased by a few hundred microns, a driven magnetic reconnection geometry forms and oppositely orientated, self-generated, MG-level magnetic fields are observed to interact with each other in a reconnection layer.

A dramatic change in the plasma dynamics is observed experimentally when the laser spot separation is increased. Increasing the laser spot separation alters the competition between the thermal plasma pressure $n_e k_B T_e$ and the magnetic pressure $B^2/2\mu_0$ at the midplane. In the lower density interaction that is created by increasing the focal spot separation, the magnetic field is more able to influence the target dynamics. Also, the Hall parameter $\omega_{ce}\tau_{ei} \gg 1$ in the corona in both cases, demonstrating that the magnetic field is able to influence electron energy transport.

One would expect an optimum laser spot separation for a given laser spot diameter and laser energy if a reconnection layer is to form. For laser spot separations of around 400 μm, lower density interactions are created and oppositely orientated magnetic fields are convected

together by the plasma flows. A current sheet necessarily forms between the two that allows the reversal of the magnetic field lines, thus creating a reconnection layer.

A number of key signatures of magnetic reconnection have been observed. Two very distinct, outflowing jets are generated in the reconnection layer. The jets propagate at around 5×10^7 cms^{-1} and are highly collimated. Thomson scattering measurements from the reconnection layer suggest > 5 keV electron temperatures in this region. This temperature is inferred from comparisons between the experimental scattered spectrum and that predicted using the standard collisionless dynamic form factor. However, such temperatures are likely to be too high and may
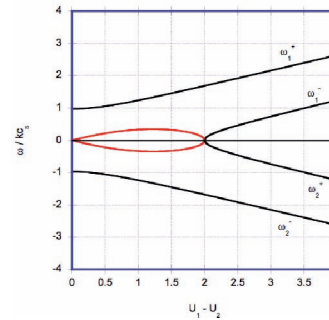

Figure 18. The ion normal modes in counterstreaming beams. The black lines are real frequencies and the red lines are imaginary frequencies of the overlapping modes. The parameters used here for illustrative purposes are $k\lambda_D = 0.25$, $n_e/n_c = 0.1$, $N_1 = N_2 = 0.5$ and $T_i = 0$.

suggest the model used to describe the plasma conditions in this region to be inadequate.

To further investigate the conditions in the interaction region we have developed a new model to interpret the TS spectrum from this region. Here we assume the presence of non-equilibrium plasma conditions in the scattering region that is not considered in the dynamical form factor of Katzenstein. The absence of magnetic fields in this interpretation is assumed. The justification and ramifications for such conjecture will be noted later.

The plasma conditions in scattering volume 2 were modelled using two dimensional simulations of an aluminium target with a hybrid code (these results are not presented in this report). The code treats the ion component subsystem kinetically while treating the electron component subsystem using a fluid approximation. Such a numerical scheme is in contrast to traditional Lagrangian hydrocodes that have been shown in numerous studies to be unable to capture the detailed physics of colliding laser-ablated plasma experiments by prematurely and artificially heating and stagnating the plasma. Thus the code can model an initial phase of interpenetration between the two interacting plasmas prior to the subsequent collision.

The code indicates that the two plasmas meet after a period of expansion and interpenetrate for some finite time prior to stagnation. Consideration of the ion modes present in counterstreaming beams was given by Powers and Berger[10]. The effect of magnetic fields on the generated modes was not considered. In this work the two counterpropagating ion beams were only considered to

interact through the ion two stream instability. The effect of this instability is to heat the ions via damping until $ZT_e/T_i > 4$ and T_i is sufficient to quench the instability. The ion acoustic modes in the plasma was shown to satisfy the dispersion relationship,

$$\varepsilon\left(\omega,\vec{k},N_1,u_1,N_2,u_2\right) = 1 + \chi_e + \sum_j N_j \chi_i\left(\omega - \vec{k}.\vec{u}_j\right) = 0 \tag{1}$$
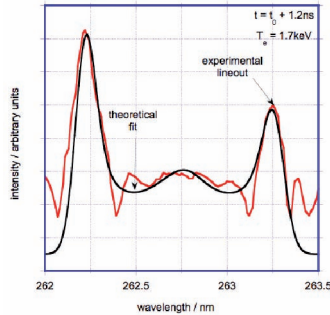

Figure 19. A lineout of the Thomson scattering spectrum (red) from scattering volume 2 at t = t$_0$ + 1.2 ns. The spectrum is fitted to that predicted using a Maxwellian electron distribution function and a non-equilibrium ion distribution function (black) giving an electron temperature T_e = 1.7 keV.

Such a dispersion relationship was derived for a system described using an ion distribution function (IDF) represented by the sum of two Maxwellians shifted by the beam flow velocity,

$$f_i(v) = \left(\frac{M}{2\pi T_i}\right) \sum_j N_j \exp\left(-\frac{M}{2T_i}\left(v - u_j\right)\right) \tag{2}$$

where the densities of the ion beams are n_1 and n_2, the flow velocities are u_1 and u_2 ($u_1 > 0$ and $u_2 < 0$ in one-dimension), the fractional beam densities are $N_j = Zn_j/n_e$, and $\chi_{e,i}$ are the electron and ion susceptibilities. The IDF is considered together with a stationary Maxwellian electron distribution function where $n_e = Z(n_1+n_2)$.

The dispersion relationship can be restated as,

$$1 + k^2\lambda_D^2 - \frac{N_1 k^2 c_s^2}{\left(\omega - \vec{k}.\vec{u}_1\right)^2} - \frac{N_2 k^2 c_s^2}{\left(\omega - \vec{k}.\vec{u}_2\right)^2} = 0 \tag{3}$$

Solutions of this dispersion relationship are plotted in figure 18, where $U = \mathbf{k.u}/kc_s$, and for illustrative purposes $k\lambda_D = 0.25$, $n_e/n_c = 0.1$, $N_1 = N_2 = 0.5$ and $T_i = 0$ (as given by Powers and Berger).

A number of features are important. In the limit of highly supersonic flow there are four ion modes with distinct frequencies. Around the sonic transition two of the four modes (ω_1^- and ω_2^+) are strongly modified. In the subsonic regime the roots of these two modes are imaginary and they lose energy to the plasma. The roots of the dispersion relationship are qualitatively the same for finite temperatures except the ion pressure alters the maximum growth rate of the modes and shifts the unstable region further into the supersonic flow regime.

An IDF consisting of two shifted Maxwellians is in great contrast to the IDF that is considered in the collisionless theory of the dynamical form factor. We have therefore used the insight provided by the results of the hybrid code

in the interpretation of the TS spectrum obtained from scattering volume 2 and included such an IDF, i.e. the sum of two shifted Maxwellians, in the calculation of the TS spectrum at $t = t_0 + 1.2$ ns, as shown in figure 19. This theoretical fit maintains the presence of a Maxwellian electron distribution function, reflecting the more mobile nature of the electron subsystem. A very good fit to the experimental data has been obtained for an electron temperature $T_e = 1.7$ keV ($T_e = T_i$, $n_e = 2.5 \times 10^{20}$ cm^{-3}) and an ion flow velocity $u_i = 2.0 \times 10^7$ cms^{-1} which is on the order of the sound velocity. The locations of the ion features are now modified by the flow velocity. These two resonances are the result of the four beam-like ion modes that are excited in the plasma caused by the interpenetrating flows. Under these experimental parameters, two of the four modes are suppressed.

The use of such an IDF is particularly novel in the interpretation of TS spectra and reconciles the very high electron temperatures that are predicted when using a standard Maxwellian IDF. However, even $T_e = 1.7$ keV is a high electron temperature given the absence of direct heating from the laser in this region. The enhanced electron temperature could result from the transfer of magnetic to thermal energy, additional collisional heating in the region of the interpenetrating plasmas, or the anomalous effects due to instabilities. Clearly the most important part of this analysis is the non-equilibrium ion distribution accounting for opposing plasma flows in the scattering (reconnection) region.

Despite the good agreement between the new theoretical model and the experimental spectra, the conditions under which such a non-equilibrium IDF is valid must be questioned. The proton deflectometry data demonstrates the presence of interacting magnetized plasmas. In this case, the two plasmas cannot interpenetrate. This is dictated by ideal MHD theory. This means that under such conditions no region can be described by this non-equilibrium distribution function. However, this IDF may be applicable if the TS diagnostic spatially integrates across the interaction region. Further, after the heater beam has turned off, the ∇T_e and ∇n_e source terms will dramatically reduce and the magnetic field generation will not be present. The plasma flows will remain and interpenetration may then occur. The non-equilibrium IDF presented here may then be appropriate.

The interaction geometry and plasma conditions presented here can be compared to the Sweet-Parker model of magnetic reconnection. For aluminium plasmas, the Alfvén velocity $v_A = 1.4 \times 10^7$ cms^{-1}. The Alfvén transit time $\tau_A = L_H/v_A = 7.4 \times 10^{-10}$ s and the resistive diffusion timescale $\tau_R = \mu_0 L_H^2 / \eta_\perp = 2.2 \times 10^{-8}$ s, assuming a hydrodynamic scalelength $L_H = 100$ μm, $T_e = 800$ eV, and $B = 1$ MG. Here, the perpendicular Spitzer resistivity $\eta_\perp = 2\eta_\parallel$ is used because the current flows perpendicular to the field. The Lundquist number $S = 30$ and the Sweet-Parker reconnection rate is given by $(\tau_A \tau_R)^{1/2} = 4$ ns. Increasing the estimate of the hydrodynamic scalelength will only increase this timescale. Thus such a reconnection rate is too slow to explain our observations and may indicate some form of anomalous resistivity in the reconnection layer. It should be noted, however, that such order of magnitude estimates introduce large errors when comparing theory and experimental observations.

Summary

In summary, we have studied for the first time a magnetic reconnection geometry in a laser-produced plasma. Key signatures of magnetic reconnection have been observed, including interacting magnetic field distributions that are driven together by plasma flows, the formation of two high velocity, collimated outflowing jets, and high electron temperatures in the reconnection layer. The jets are observed to propagate at approximately the Alfvén velocity at an angle to the target surface, indicating a complex three dimensional interplay between the $\nabla T_e \times \nabla n_e$ field distributions. Radiation cooling is also observed to influence the jet collimation in higher-Z target interactions.

References
1. D. Biskamp, *Physics Of Fluids* **29**, 5 (1986)
2. H. T. Ji, *et al.*, *Physics Of Plasmas* **6**, 5 (1995)
3. H. T. Ji, *et al.*, *Physical Review Letters* **80**, 15 (1998)
4. R. M. Kulsrud, *Earth Planets And Space* **53**, 6 (2001)
5. J. A. Goetz, R.N. Dexter, and S.C. Prager, *Physical Review Letters,* **66**, 5 (1991)
6. T. D. Phan, *et al.*, *Nature* **439**, 7073 (2006)
7. S. H. Glenzer, **et al**., *Physical Review Letters* **79**, 7 (1997)
8. G. Gregori, *et al.*, *Physical Review Letters* **92**, 20 (2004)
9. W. Rozmus, *et al.*, *Astrophysical Journal Supplement Series*, **127**, 2 (2000)
10. L. V. Powers and R.L. Berger, *Physics Of Fluids* **31**, 10 (1988)